Experimental results of the gamma-ray imaging capability with a Si/CdTe semiconductor Compton camera

Shin'ichiro Takeda, Hiroyuki Aono, Sho Okuyama, Shin-nosuke Ishikawa, Hirokazu Odaka, Shin Watanabe, Motohide Kokubun, Tadayuki Takahashi, Kazuhiro Nakazawa, Hiro Tajima, Naoki Kawachi

***Abstract*—A semiconductor Compton camera that combines silicon (Si) and Cadmium Telluride (CdTe) detectors was developed, and its imaging capability was examined with various kinds of gamma-ray targets such as a point source, arranged point sources and an extended source. The camera consists of one double-sided Si strip detector and four layers of CdTe pad detectors, and was designed to minimize the distance between a scatterer and the target. This is because the spatial resolution with Compton imaging improves as the target approaches the scatterer. This new camera realizes a minimum distance of 25 mm. By placing the target at a distance of 30 mm from the detector, resolving power better than 3 mm was demonstrated experimentally for a 364 keV (^{131}I) gamma-ray. Positional determination with accuracy of 1 mm was also demonstrated. As a deconvolution method, we selected the iteration algorithm (called List-Mode Expectation-Maximizing Maximum Likelihood), and applied it to several kinds of experimental data. The Compton back projection images of the arranged point sources and an extended object were successfully deconvolved.**

***Index Terms*—Gamma-ray imaging, Silicon strip detector, CdTe detector, Compton Camera**

I. Introduction

COMPTON imaging is an attractive technology used in gamma-ray detection for various applications. In high energy astrophysics, high-sensitivity gamma-ray observation is required for studying nucleosynthesis and particle acceleration, the phenomena of which are widely observed throughout the vast universe. The technology is also applicable to nuclear medical imaging and/or non-destructive inspection [1] [2], since it can directly locate the position of gamma-ray signals with a wide field of view, as well as a wide energy band.

We have developed a Compton camera – the Si/CdTe Compton camera [3]–[6] – based on the combination of Silicon (Si) and Cadmium Telluride (CdTe) semiconductor detectors. It consists of many layers of thin Si and CdTe position-sensitive detectors. The design leads to a high-angular resolution thanks to the high-energy and position resolution of these semiconductor detectors, including dedicated low-noise analog ASICs. Si is a suitable scatterer material, given its smaller Doppler broadening effect than that of any other semiconductor devices [7]. This effect is caused by the non-zero momenta of electrons, and imposes a theoretical limit on angular resolution. CdTe works very nicely as an absorber thanks to its large atomic numbers (48, 52) and high density (5.8 g/cm^3).

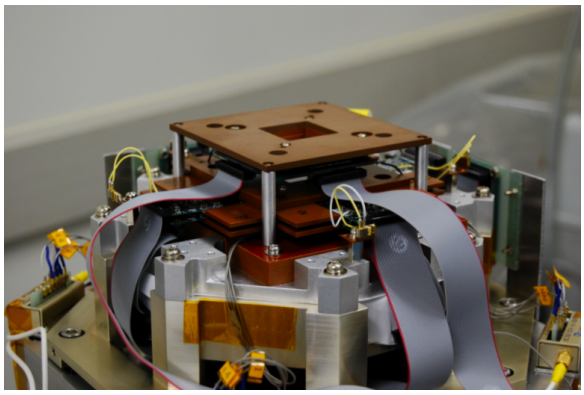

Fig. 1. Photograph of the Compton Camera

In our previous work, we developed a prototype Compton camera that was primarily designed for future balloon-borne astrophysics experiments [8], and verified its performance. The Compton reconstruction was successfully performed and the gamma-ray images of point sources were obtained from 662 keV down to 59.5 keV. The typical resolution of scattering angle (the Angular Resolution Measure or ARM) was 3.5 $^\circ$ Full-Width-at-Half-Maximum (FWHM) and 2.5 $^\circ$ (FWHM) at 356 keV and 511 keV, respectively.

A Compton camera with an angular resolution of a few degrees is an attractive detector applicable not only to astrophysics, but also to nuclear medical imaging. Such applications require spatial resolution at the mm level. In this paper, we report the experimental results of Compton imaging using a new detector designed for high spatial resolution in short-distance imaging. Fig.1 shows a photo of the detector system. Section II describes our approach to obtaining high spatial resolution. Section III describes the key detectors mounted on the Compton camera and the camera's design. Section IV

S. Takeda, H. Aono, S. Ishikawa, H. Odaka, S. Watanabe, M. Kokubun, and T. Takahashi are members of the Institute of Space and Astronautical Science, Japan Aerospace Exploration Agency, Kanagawa 229-8510, Japan, and also the department of physics, University of Tokyo, Tokyo 113-0033, Japan (e-mail: takeda@astro.isas.jaxa.jp)

S. Okuyama and K. Nakazawa are members of department of physics, University of Tokyo.

H. Tajima is with the Stanford Linear Accelerator Center in Menlo Park, CA 94025 USA.

N. Kawachi is from the Quantum Beam Science Directorate, Japan Atomic Energy Agency, 1233 Watanuki, Takasaki, Gunma 370-1292, Japan.

This work was supported in part by Gumma University's Faculty of Medicine and the Japan Atomic Energy Agency under grant JSPS COE (biomedical research using accelerator technology).

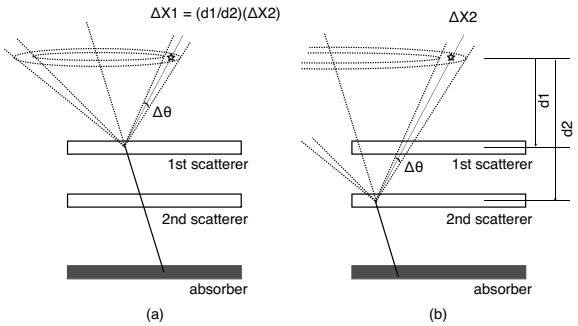

Fig. 2. Schematic of a Compton camera consisting of two scatterers and one absorber. Case (a) has a factor of (d1/d2) better spatial resolution, as derived from the angular resolution multiplied by the distance.

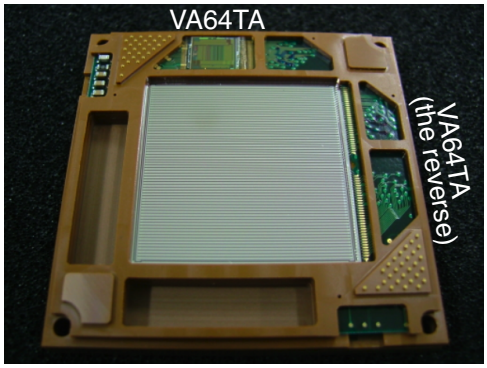

Fig. 3. Photograph of a DSSD board

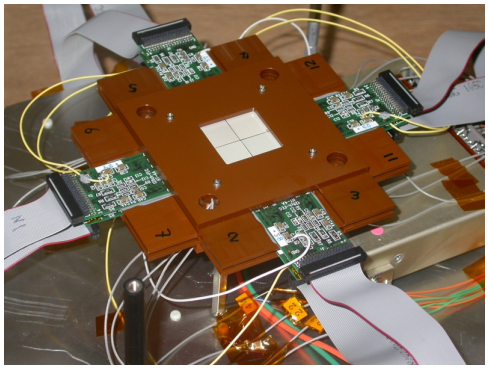

Fig. 4. Photograph of a 4-layer stacked CdTe module

describes the procedure of Compton imaging, and Section V summarizes the imaging results.

II. Design Approach to High Spatial Resolution

In order to achieve the high spatial resolution of a short-distance target by using Compton imaging, designing the arrangement of detectors requires special care. Fig. 2 shows the schematic of a Compton camera consisting of two scatterers and one absorber. A gamma-ray photon emitted from a target is detected through two major scenarios: (a) scattered in the 1st scatterer or (b) in the 2nd scatterer, and then absorbed in the absorber detector. The direction of incident photons is obtained as a cone in the sky (Compton cone) based on information about the interaction positions and related energy deposits in both the scatterer and absorber. By simply assuming that cases (a) and (b) have the same angular resolution, case (a) has a factor of (d1/d2) better spatial resolution, as derived from the angular resolution multiplied by the distance. Generally speaking, the spatial resolution in Compton imaging gradually deteriorates as the distance increases between the target and scatterer.

In our previous Compton camera [8], we used a Si scatterer consisting of four layers of a double-sided silicon strip detector (DSSD described in Section III-A) in order to improve detection efficiency [8] [9]. For astrophysical imaging, only the angular resolution and detection efficiency are essential since the targets are located virtually indefinitely in the far distance. Conversely, in a short-distance application, the 2nd to 4th layer of the scatterer degrades the spatial resolution, given the increasing distance to the target. Therefore, we employed one DSSD layer for the scatterer in the Compton camera described in this paper. It is also important to minimize the distance between 1st scatterer and a target. When considering the few degrees of angular resolution, the interval must be limited within a few tens of mm to obtain mm-scale spatial resolution. In our case, a minimum distance of 25 mm to a target was achieved.

III. Compton Camera Setup

A. Double-sided silicon strip detector (DSSD)

As a scattering part of the Compton camera, we developed a low-noise double-sided silicon strip detector (DSSD) [9]–[12]. Fig. 3 shows a photograph of the DSSD board. It consists of one DSSD and two low-noise, low-power consumption analog VLSIs (VA64TA1s [13] developed in collaboration with Gamma-Medica Ideas) and mounted on a small circuit board. The DSSD used here is a 2.56-cm wide and 500-μm thick device developed in conjunction with Hamamatsu Photonics, Japan. The strip pitch is 400 μm with a strip gap of 100 μm on each side. The N-side has a floating p-implantation between the strips to isolate the adjacent strips. The Al electrodes are directly coupled on each strip with ohmic contact.

In order to extend the imaging band down to low-energy gamma-rays, low-noise read-out to achieve a lower detection threshold is needed on both the P-side and N-side strips of the DSSD. This is because we need both the P-side and N-side signals to obtain two-dimensional positional information. Thus, a DC-coupled readout is employed for both sides. To apply a reverse bias, the N-side circuit board is biased as a whole. The applied bias voltage is 250 V. The decoupling is held on the digital interface after the analog signal is digitalized by the ADC. The energy resolution at 59.5 keV is found to be 1.6 keV (FWHM) for the P-side and 2.8 keV for the N-side. From the noise level measured on the N-side, we calculated the possibility of incorrectly identifying the position due to random noise, and found that it is less than 10% for a 5 keV energy deposit for this device.

B. 4-layer stacked CdTe module

The absorber consists of a total 16 CdTe pad detectors based on the technology of a high-resolution CdTe Schottky diode [14]–[16]. The production and pixelation of CdTe were performed by ACRORAD, Japan. Each detector is 13.2-mm wide and 500-μm thick. In the CdTe detector, a common electrode made of Indium (In) is used as the anode, and pixelated electrodes divided into 64 pads made of Platinum (Pt) are used as the cathode. The size of each pad of the cathode electrode is 1.35 mm^2, with a gap of 50 μm between the electrodes. A guard-ring electrode surrounds the pads. Due to a high Schottky barrier and the guard-ring electrode, leakage current as low as 10 pA per pad is obtained under bias voltage of 700 V. Good energy resolution is realized thanks to the higher efficiency of charge collection.

Fig. 4 shows the 4-layer stacked CdTe module with a stack pitch of 2 mm [16]. One layer consists of four CdTe pad detectors configured in 2×2 geometry and two FECs (Front End Cards) on which four VA64TA1s are mounted. Energy resolution of 2.0 keV (FWHM) is achieved at 81 keV and that of ΔE/E $\sim$1% (FWHM) is at 511 keV under temperature of –20°C, and bias voltage of 600 V. Under these conditions, no significant degradation in spectrum performance was observed during continuous operation of up to two weeks.

C. Setup of the Compton camera

We constructed the new Compton camera (shown in Fig.1) by combining the DSSD and 4-layer stacked CdTe module. Fig. 5 shows a cross-sectional view of the camera. The 4-layer stacked CdTe module is arranged 14.7 mm underneath the DSSD. The minimum distance to the target (d_{min}) is 25 mm due to the entrance window provided for thermal decoupling.

Fig. 6 shows a schematic diagram of the readout system. The readout VA64TA1s are divided into four groups: DSSD Pside, DSSD Nside, CdTe-A, and CdTe-B. In the CdTe-A and CdTe-B groups, the eight VA64TA1s are arranged in a daisy chain configuration. The readout sequence of each group is controlled by a dedicated Read Out CTL Unit (ROU). The ROU starts the readout sequence by using an external read start trigger. The event trigger from the Compton camera is fed to the TRIG CTL Unit (TCU) that consists of NIM modules in this version. In the TCU, a coincidence judgment is made between the trigger of DSSD and that of CdTe for the effective acquisition of data on Compton events. The coincidence judgment output is then returned to the ROU as a read start trigger. Since this trigger is sent to all ROUs, the pulse heights of all channels are acquired for a coincidence event. The pulse heights converted into digital data in the ROU are then sent to DATA&Command Unit controlled by a PC via the VME bus.

IV. Procedure for Compton imaging

Data reduction and image reconstruction are performed for Compton imaging. First we select "two hit events", meaning one hit in a DSSD and one in a CdTe detector. Here, the energy threshold to determine a hit is set to 10 keV for both the DSSD and CdTe detectors. Obtaining the Compton events of

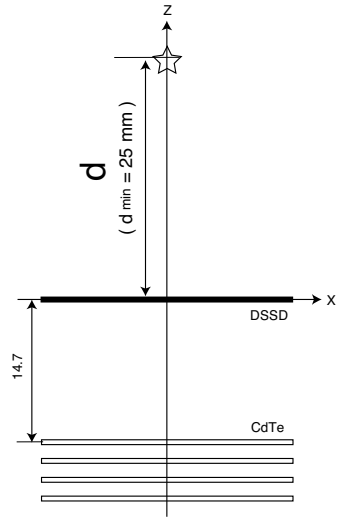

Fig. 5. Cross-sectional view of the Compton camera

incident gamma-rays entails the selection of "two hit events" as follows:

- The sum of energy deposits in Si (E_{dssd}) and CdTe (E_{cdte}) is equal to the incident gamma-ray energy (E_{in}), that is, $E_{\rm dssd} + E_{\rm cdte} = E_{\rm in}$. By considering the energy resolution of the detectors, the events where $E_{\rm dssd}+E_{\rm cdte}$ equal $E_{\rm in} \pm 5$ keV are selected.
- The events where $E_{\rm dssd}$ is from 20 keV to 35 keV are excluded. This region is contaminated by fluorescence X-ray events, which are X-rays from Cd (K_α : 23.1 keV, K_β : 26.1 keV) and Te (K_α : 27.4 keV, K_β : 31.0 keV) escaping from the CdTe detectors and then absorbed in the DSSD.

With these selected events, the Simple Back Projection (SBP) image was obtained. We assumed that incident gamma-rays are scattered in the DSSD and absorbed in the CdTe detector. Based on this assumption, the direction of incident photons is calculated as;

$$\cos\theta = 1 - m_e c^2 \left(\frac{1}{E_{\rm cdte}} - \frac{1}{E_{\rm dssd} + E_{\rm cdte}}\right). \qquad (1)$$

The back projection of the Compton cone into the RI source plane is performed event by event. The SBP image is the simple accumulation of Compton cones over all events. The overlapping position of the Compton cones is the origin of the gamma-rays.

Conversely, in the SBP image, most parts of a cone not overlapping with a source become the background. Imaging capability should be improved using a deconvolution method that properly accounts for the response of the Compton camera. We selected a deconvolution algorithm called List-Mode Expectation-Maximizing Maximum Likelihood (LM-EM-ML). Briefly, this is an iteration algorithm between image space and data space.

$$\lambda_j^{l+1} = \frac{\lambda_j^l}{s_j} \sum_i \frac{t_{ij}}{\sum_k t_{ik} \lambda_k^l} \qquad (2)$$

where, λ_j^l denotes the image-bin content at iteration level l, s_j the probability that an event emitted from j is measured, and

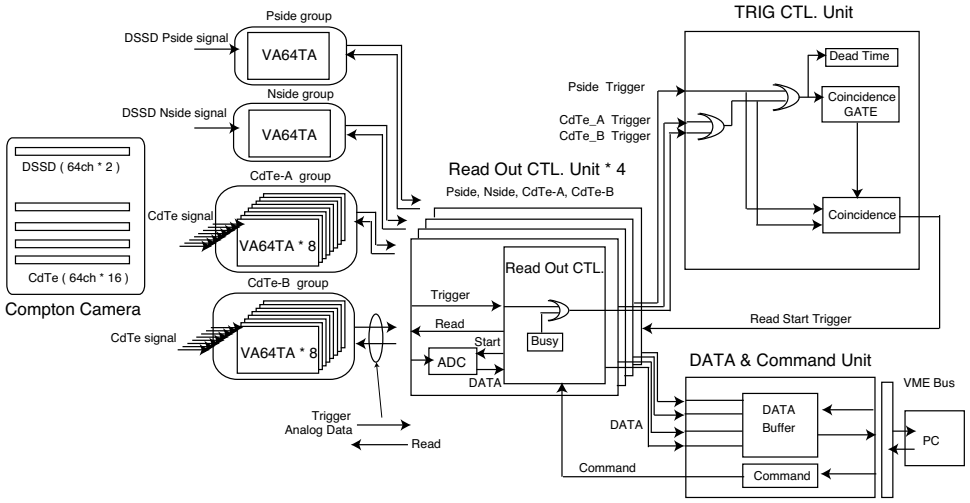

Fig. 6. Schematic diagram of the readout system

t_{ij} the probability that a photon emitted from j is measured with the parameters of event i (response). From image space, estimated data space is calculated with a response matrix derived from list-mode data. By comparing the expected data and measured data, corrections are made to image space. A detailed description of the LM-EM-ML method is given in [17], [18].

V. Results

A. Distance dependence

As mentioned in Section II, the spatial resolution is a function of the distance between the scatterer and target. To demonstrate this concept, we obtained point source data in three cases of d = 30 mm, 60 mm and 150 mm. Here, d denotes the distance between the DSSD and the point source, as shown in Fig. 5. The 356 keV gamma-ray source is placed on the Z-axis penetrating the center of the DSSD.

The left panel in Fig. 7 shows the distance dependence of spatial resolution of the SBP image; the right panel shows that of the angular resolution defined by FWHM of the ARM distribution. We evaluated the spatial resolution as FWHM of the SBP image by fitting using a two-dimensional Voigt function. The function is a convolution of Gaussian and Lorentzian distribution, and offers good approximation of a point spread function. We also determined the angular resolution as the ARM distribution in FWHM, by using a one-dimensional Voigt function. The obtained angular resolution was 3.6 ° and independent of the distance. The spatial resolution (proportional to distance) was about 6 mm and 18 mm at d = 30 mm and d = 150 mm, respectively. This relation is consistent with the description given in Section II.

B. Field of view

One feature of Compton imaging is a wide field of view. By using 356 keV and 511 keV gamma-ray point sources, we investigated the position dependence relative to detection efficiency. The point source was placed on the plane of d = 60 mm (see Fig. 5), and measurements were performed for several

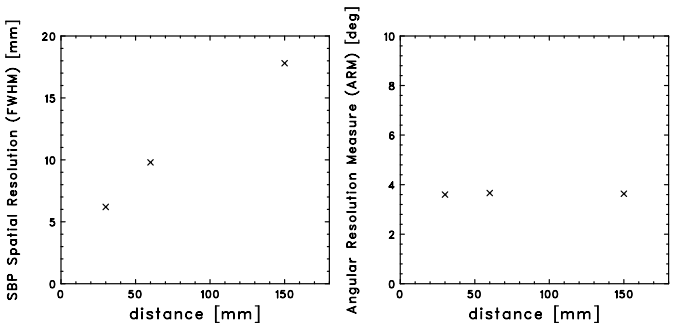

Fig. 7. Left panel showing the distance dependence of spatial resolution of the SBP image; right panel showing that of angular resolution defined by FWHM of the ARM distribution for a 356 keV gamma-ray.

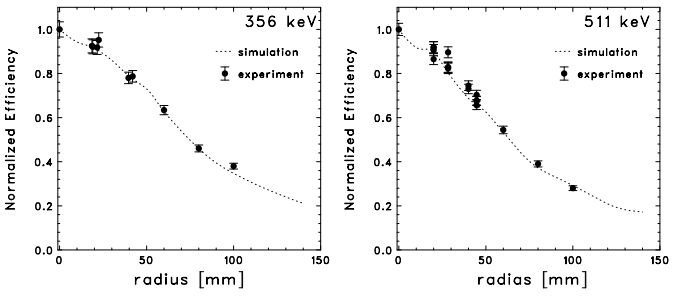

Fig. 8. The position dependence of detection efficiency for 356 keV and 511 keV at d = 60 mm plane. The efficiency at the center position (x,y,z) = (0,0,60) in Fig. 5 is set to 1. The radius denotes the distance from (x,y) = (0,0). The radius 100 mm corresponds to a 120° field of view.

positions on the plane. The detection efficiency for each position is obtained from the counts of events where the total energy deposit (E_{DSSD} + E_{CdTe}) is within 356 keV±5 keV or 511 keV±5 keV.

Fig. 8 shows the position dependence of detection efficiency normalized at the center position of (x,y,z) = (0,0,60) for the 356 keV (left) and the 511 keV (right) gamma-rays. The radius denotes the distance from (x,y) = (0,0). The normalized efficiency at a radius of 100 mm (corresponding to a 120° field of view) is 40 % for 356 keV and 30 % for 511 keV.

For a detailed evaluation of detection efficiency, we developed a simulator [19] based on the Geant4 toolkit. In the simulation, we included the G4LECS [20] extension in order to estimate the effect of Doppler broadening. The mass model is constructed not only with the detector material, but also with various passive support structures. The energy and position resolutions of the detectors are parameterized based on the experimental results. Fig. 8 shows the normalized efficiency calculated by the simulator, together with the experimental data. The simulation reproduced the experimental results very well. The absolute efficiency derived from the simulator is on the order of 10^{-2} % at the center position for 356 keV gamma-rays.

C. Imaging of grid sources

To investigate the resolving power and accuracy of positional determination, an imaging test was conducted using an acrylic plate with 2 mm diameter holes arranged regularly (Fig. 9). The liquid ^{131}I (364 keV, 85 kBq/hole) sources were mounted at 20-mm pitch. The variability of strength of each source is less than 10 %. Imaging is performed in three cases: d = 30, 45 and 60 mm.

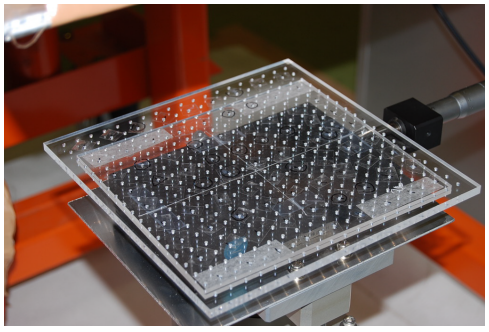

Fig. 9. Acrylic plate with 2 mm diameter holes arranged regularly. The liquid ^{131}I (364 keV) sources were mounted at 20-mm pitch.

Fig. 10 summarizes the SBP images. The point sources were clearly resolved. The outside sources become visible as d increases, since the sources enter the field of view. Resolving power better than 20 mm was demonstrated up to a distance of d = 60 mm, and larger than an 80° field of view as well.

We performed image deconvolution by using the LM-EM-ML method. A total of 1×10^5 events are utilized in this process. A correction factor (s_j) in Equation 2 is derived from the position dependence of detection efficiency calculated by the simulator mentioned in Section V-B. Fig. 11 shows the deconvolution results for the experimental data obtained at d = 60 mm. The left panel shows the SBP image; the right panel shows the deconvolved image after the 100th iteration. In the deconvolved image, the point sources placed at the edge become apparent, while only sources located around the central region are resolvable in the SBP image. The bottom panel is the projection of the rectangular region shown in each image to the Y-axis in Fig. 11. Following deconvolution, the peak area of each source becomes stable, thanks to the deconvolution technique that included the correction of efficiency.

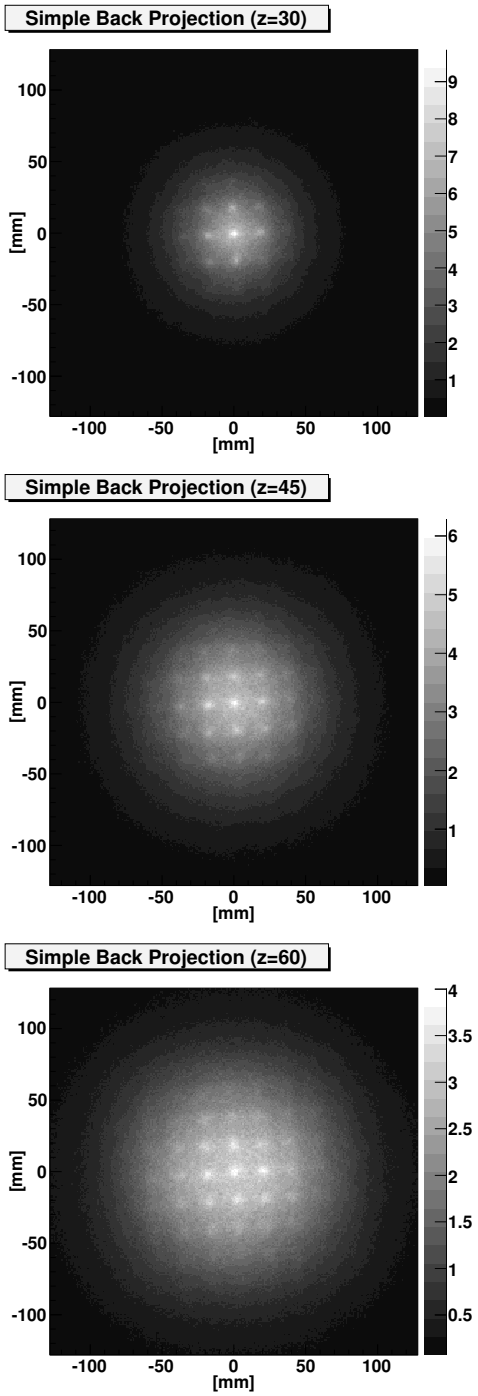

Fig. 10. SBP image of the grid sources in case of d = 30 (top), 45 (center) and 60 (bottom) mm. The liquid ^{131}I (364 keV) sources were mounted with a pitch of 20 mm.

It is also important to study the accuracy of positional determination. Therefore, we first derived the center position of the sources from the deconvolved image shown in the right panel in Fig. 11. For the 25 sources arranged in 5×5, the center position of each source was determined by calculating the weighted center around the largest pixel. The center positions are plotted as shown Fig. 12 with open squares. Then based on the assumption that the sources are at the intersection of

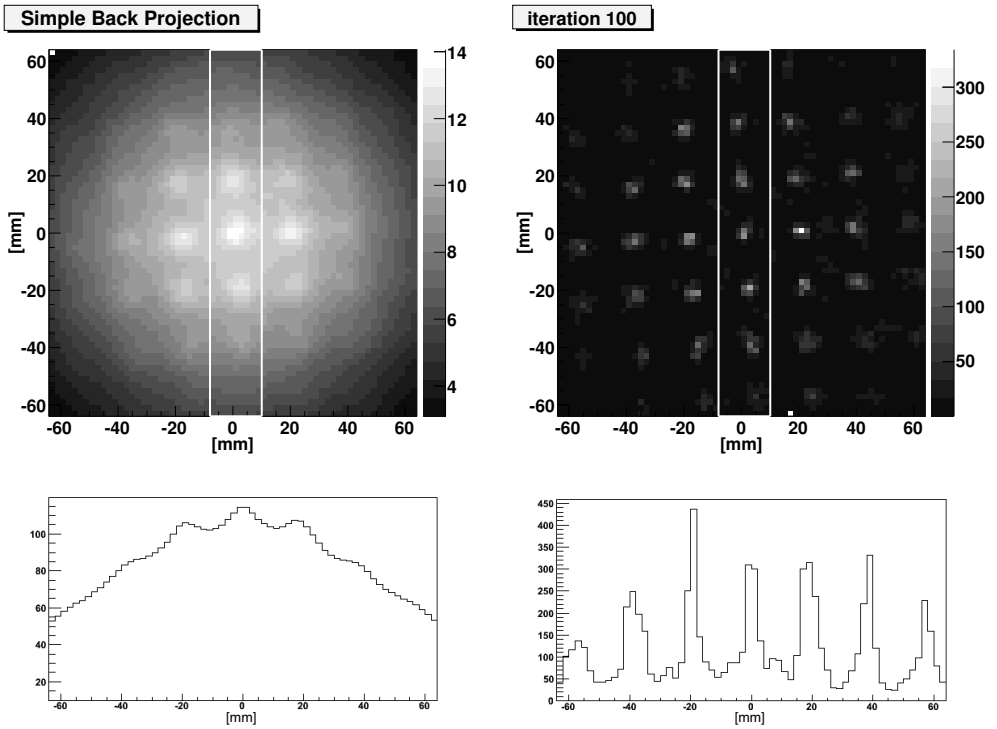

Fig. 11. Deconvolution results for experimental data (d = 60 mm in Fig. 10). The left panel shows the SBP image; the right panel shows the deconvolved image after the 100th iteration. The bottom panel is the projection of the rectangular region of each image to the Y-axis.

cross lines at a right angle, we fit the center positions. The red grid in Fig. 12 shows the fitting results. The bottom panel of Fig.12 summarizes the differences of these positions of all 25 sources as distributed within $\sim$1 mm. Thus, this experiment demonstrates positional determination accuracy of 1 mm for the point source.

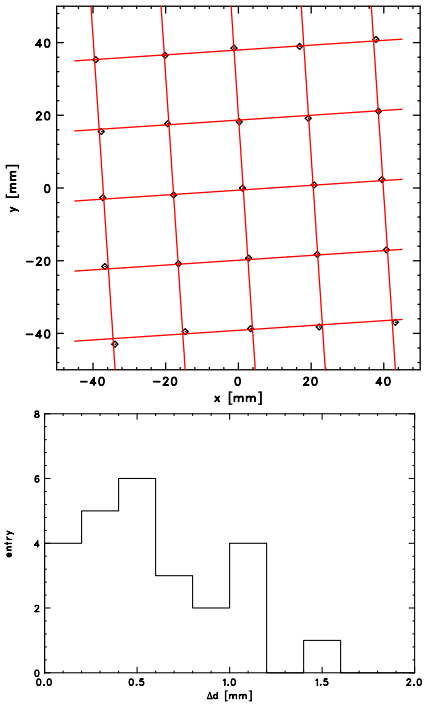

Fig. 12. Top: measurement values of source positions (open square) derived from the deconvolved image shown in the right panel of Fig. 11 in the grid (cross lines). Bottom: distribution of the difference of all 25 sources.

D. Extended object

Since the ability to image extended object is a key requirement for both astrophysical and medical applications, we prepared an extended target as shown in Fig.13. The liquid ^{131}I source (364 keV, 1.6 MBq) is soaked in paper and shaped like an inverted "C" with a gap of 3 mm. The target was placed on the d = 30 mm plane.

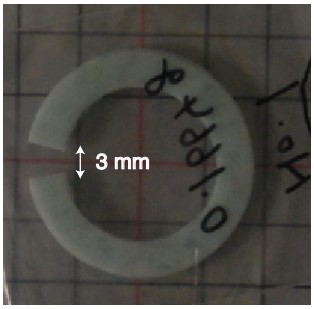

Fig. 13. Photograph of the extended target. The liquid ^{131}I source in soaked in paper, and shaped like an inverted "C" with a gap of 3 mm.

Fig. 14 shows the images obtained. The top panel shows the SBP image; the bottom panel shows the 10th iteration using the LM-EM-ML method. The shape with a gap of 3 mm is recognized even in the SBP image. With the LM-EM-ML method, the shape is successfully deconvolved. Thus, resolving power better than 3 mm is demonstrated experimentally.

VI. Conclusion

By combining the DSSD and a 4-layer stacked CdTe module, we developed a new Compton camera designed to achieve high spatial resolution. As explained in Section II, the spatial resolution gradually deteriorates as the distance increases between the target and scatterer. Therefore, the camera is designed to minimize this distance. A minimum distance of 25 mm was realized. Studies were conducted on the field of view, spatial resolution, the accuracy of positional determination, and resolving power. Using the experimental data, resolving power better than 3 mm was demonstrated for a 364 keV (^{131}I) gamma-ray placed 30 mm away from the sensor. Positional determination accuracy of 1 mm was also demonstrated experimentally. Furthermore, the imaging of an extended object was also successfully performed.

As the deconvolution method, we selected an iteration algorithm called List-Mode Expectation-Maximizing Maximum Likelihood (LM-EM-ML). It was applied to several kinds of experimental data. The Compton back projection images derived from the arranged point sources and the extended object were successfully deconvolved.

The results of this imaging test suggest that the Si/CdTe Compton camera is an attractive detector not only for astrophysics application, but also for medical imaging. The data obtained by the experiments also proved effective in investigating the detailed response of a Compton camera used in astrophysics.

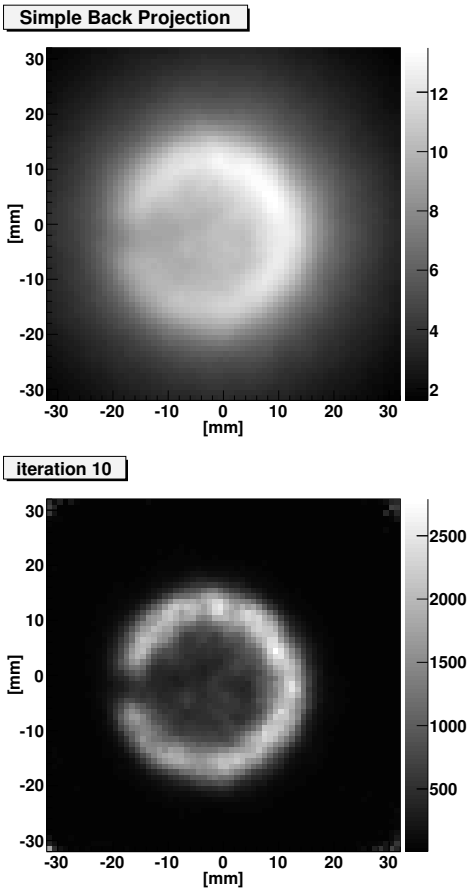

Fig. 14. Results of extended target imaging. The distance to the target is d = 30 mm. The top panel shows the SBP image; the bottom panel shows the deconvolved image after the 10th iteration.

References

[1] R.W.Todd et al., Nature, vol. 251, pp. 132-134 1974
[2] M.Singh et al., Med. Phys, vol. 10, no. 4, pp. 428-435, 1983
[3] T. Takahashi et al., in Proc. SPIE-Int. Soc. Opt. Eng., vol.4851, pp. 1228-1235, 2003.
[4] T. Mitani et al., IEEE Trans. Nucl. Sci., vol. 51, no. 5, pp. 2432-2437, 2004
[5] T. Tanaka et al. , Nucl. Instr. and Meth. A., vol. 568, pp. 375-381, 2006.
[6] S. Watanabe et al. , IEEE Trans. Nucl. Sci. vol. 52, no. 5, pp. 2045-2051, 2005.
[7] A. Zoglauer et al., in Proc. SPIE-Int. Soc. Opt. Eng., vol. 4851, pp. 1302-1309, 2003.
[8] S. Takeda et al. Proc. SPIE, vol. 6706, 67060S
[9] S.Takeda et al. SPIE newsroom, http://spie.org/x20060.xml 2008.
[10] K. Nakazawa et al., Nucl. Instr. and Meth. A., vol. 573, pp. 44, 2007.
[11] H. Tajima et al., in Proc. SPIE-Int. Soc. Opt. Eng., vol. 4851, pp. 875-884, 2003.
[12] S. Takeda et al., Nucl. Instr. Meth., A., vol 579/2., pp. 859-865, 2007.
[13] T. Tanaka et al., Nucl. Instr. Meth., A., vol 568., pp. 375-381, 2006.
[14] T. Takahash et al., IEEE trans. Nucl. Sci., vol. 49, no. 3, pp.1297-1303, 2002.
[15] K. Nakazawa et al., IEEE trans. Nucl. Sci. NS-51 (4) 1881, 2004.
[16] S. Watanabe et al., Nucl. Instr. Meth., A., vol. 579/2 pp. 871-877, 2007.
[17] S. Wilderman et al., IEEE Nucl. Sci.Sympo. vol.3 pp.1716–1720 1998
[18] A. Zoglauer, PhD thesis, Technische Universitat Munchen 2005
[19] H. Odaka et al. Nucl. Instr. Meth., A., vol 579/2., pp. 878-885, 2007.
[20] G4LECS http://public.lanl.gov/mkippen/actsim/g4lecs/ .